Measuring 3-D Surface Motion With Future SAR Systems Based on Reflector Antennae

Homa Ansari, Francesco De Zan, Alessandro Parizzi, Michael Eineder, *Senior Member, IEEE*, Kanika Goel, and Nico Adam

***Abstract*—A conventional interferometric synthetic aperture radar (SAR) system provides 1-D line-of-sight motion measurements from repeat-pass observations. Two-dimensional motions may be measured by combining two observations from ascending and descending geometries. The third motion component may be retrieved by adding a third geometry and/or by integrating along-track measurements although with much reduced precision compared to the other two components. Several options exist to improve the accuracy of retrieving the third motion component, such as combining left- and right-looking observations or exploiting recently proposed innovative SAR acquisition modes (BiDiSAR and SuperSAR). These options are, however, challenging for future SAR systems based on large reflector antennae, due to lack of capability to electronic beam steering or frequent toggle between left- and right-looking modes. Therefore, in this letter, we assess and compare the realistic acquisition scenarios for a reflector-based SAR in an attempt to optimize the achievable 3-D precision. Investigating the squinted SAR geometry as one of the feasible scenarios, we show that a squint of 13.5° will yield comparable performance to the left-looking acquisition, while further squinting outperforms this or other feasible configurations. As an optimum configuration for 3-D retrieval, the squinted acquisition is further elaborated: the different acquisition plans considering a constellation of two satellites as well as the challenges for data processing are addressed.**

***Index Terms*—Azimuth shifts, error analysis, interferometric SAR (InSAR), SAR acquisition geometry, squinted SAR, 3-D surface motion.**

I. Introduction

INTERFEROMETRIC synthetic aperture radar (InSAR) has proved to be a precise geodetic tool in Earth deformation monitoring. This technique, however, merely allows capturing the projection of the actual 3-D surface motion onto the line of sight (LOS) direction of the sensor. The observed 1-D motion is rather blind to the motion in the along-track direction (ATD) of the satellite. This blindness hinders the retrieval of precise 3-D motion. The 3-D surface monitoring is of utmost importance in precise/unambiguous modeling of geophysical phenomena, such as seismic and volcanic activities, as well as precise model-free deformation monitoring [1]–[6]. This importance has led the geophysical community of SAR users toward 3-D retrieval of the surface motion [5]. In previous studies, the fusion of LOS measurements from different acquisition geometries and/or with the differential SAR image shifts in ATD has been proposed as a solution. However, equal-precision 3-D motion estimation cannot be achieved; specifically, the precision in the north direction is severely compromised. To improve this precision, the fusion of InSAR measurements acquired from right- and left-looking geometries on both ascending and descending passes (hereafter referred to as *cross-heading tracks*) was suggested [1], [2]. Although enhancing the precision, the left-looking acquisition requires extreme attitude maneuver which is critical for satellites with large reflector antenna. Moreover, despite improvement, this configuration does not allow the retrieval of north motion with a precision comparable to the other two motion components. This fact calls for the investigation of alternative acquisition geometries.

InSAR 3-D performance is merely related to the imaging geometry of the combined acquisitions, defined by the satellite heading and antenna look angle. The higher is the angular diversity among the combined acquisitions, the more precise would be the 3-D retrieval. There are two options to improve the angular diversity. One is combining acquisitions from different look angles; in this regard, the left-looking configuration provides the maximum angular diversity when combined with the right-looking. The second possibility is alteration of the heading angle, which consequently improves the sensitivity of the acquisitions to the north motion. As it will be shown, the latter has a greater impact on improving the 3-D performance but has consequences for the orbit design. A comparable effect to heading angle alteration can be achieved by squinted acquisition. There are several proposals (BiDiSAR [7] and SuperSAR [6]) focused on the squinted SAR via the so-called *bidirectional* imaging mode which enables simultaneous acquisition of fore- and backward-looking images. However, future SAR systems based on large reflector antennae, such as DLR's TanDEM-L proposal [8], will not be capable of this acquisition mode. The focus of this letter is on investigation of the advantages of the squinted SAR for such systems in a conventional stripmap acquisition mode while addressing and comparing to the other geometrical and data fusion possibilities.

II. InSAR in 3-D Motion Retrieval

The LOS motion observed by InSAR can be expressed as the inner product of the following: $d_{\mathrm{LOS}} = \boldsymbol{e}_{\mathrm{LOS}} \cdot \boldsymbol{d}$, where $\boldsymbol{d}$ is the 3-D motion vector in the local east–north–vertical system: $\boldsymbol{d} = [d_e, d_n, d_v]^T$ and $\boldsymbol{e}_{\mathrm{LOS}}$ is the LOS unit vector. The latter is a function of the antenna orientation, i.e., the heading α and look angle θ.

Manuscript received July 14, 2015; revised November 30, 2015; accepted December 1, 2015. Date of publication January 7, 2016; date of current version January 19, 2016. This work was supported by the German Helmholtz Alliance on "Remote Sensing and Earth System Dynamics."

The authors are with German Aerospace Center (DLR), 82234 Wessling, Germany (e-mail: homa.ansari@dlr.de; francesco.dezan@dlr.de; alessandro.parizzi@dlr.de; michael.eineder@dlr.de; kanika.goel@dlr.de; nico.adam@dlr.de).

Color versions of one or more of the figures in this paper are available online at http://ieeexplore.ieee.org.

Digital Object Identifier 10.1109/LGRS.2015.2509440

ATD motion may also be obtained by the differential image shifts in azimuth direction, hereafter referred to as the *azimuth shifts*, although with a much lower precision compared to InSAR. These measurements can be obtained by various techniques such as cross-correlation, exploitation of spectral diversity [9], [10], etc. In this case, the 3-D motion is mapped as follows: $d_{\mathrm{ALD}} = \boldsymbol{e}_{\mathrm{ALD}} \cdot \boldsymbol{d}$, where $\boldsymbol{e}_{\mathrm{ALD}}$ is the ATD unit vector, as a function of the local heading angle α.

Introducing the functional model $\boldsymbol{y} = A \cdot \boldsymbol{d}$, where vector $\boldsymbol{y}$ contains the observed motion and matrix A is defined by the respective measurements' direction, i.e.,

$$\begin{aligned} y_i &= (d_{\mathrm{ALD},i} \ \text{ or } \ d_{\mathrm{LOS},i}) \\ \boldsymbol{a}_i &= [\boldsymbol{e}_{\mathrm{ALD},i} \ \text{ or } \ \boldsymbol{e}_{\mathrm{LOS},i}] \\ A &= [\boldsymbol{a}_1, \boldsymbol{a}_2, \ldots, \boldsymbol{a}_n]^T \end{aligned}$$

the 3-D motion is retrieved by weighted least squares as follows:

$$\boldsymbol{d} = \left(A^T Q_y^{-1} A\right)^{-1} A^T Q_y^{-1} \boldsymbol{y}. \tag{1}$$

Here, Q_y is the covariance matrix introducing the measurements' stochastic model, approximated by the Cramér–Rao bounds of interferometric [11] and azimuth shift [12] measurements, i.e.,

$$\sigma^2_{0,\mathrm{LOS}} = \frac{1-\gamma^2}{2N\gamma^2}\left(\frac{\lambda}{4\pi}\right)^2 + \sigma^2_{\mathrm{APS}} \tag{2}$$

$$\sigma^2_{0,\mathrm{ATD}} = \frac{3}{2N} \cdot \frac{1-\gamma^2}{(\pi.\gamma)^2} \cdot \rho^2_{az} \tag{3}$$

respectively. Here, γ is introduced as signal coherence, N is the number of samples exploited in the estimation of the measurements, ρ_{az} is the SAR resolution in azimuth direction, λ is the SAR wavelength, and σ_{APS} represents the atmospheric errors.

Having this setup, the 3-D estimation covariance matrix can be utilized as the statistical measure for assessing the 3-D performance:

$$Q_d = \left(A^T Q_y^{-1} A\right)^{-1} = \begin{bmatrix} \sigma_e^2 & \sigma_{en} & \sigma_{ev} \\ \sigma_{en} & \sigma_n^2 & \sigma_{nv} \\ \sigma_{ev} & \sigma_{nv} & \sigma_v^2 \end{bmatrix}. \tag{4}$$

Q_d is a square symmetric matrix serving as the initial point of error assessment: with its diagonal elements representing the estimation error variance and its 2×2 submatrices representing the second-order statistics of joint bivariate probability density function (pdf) between the parameter pairs. Assuming Gaussian stochastics, the joint pdfs are further visualized as follows: applying the eigendecomposition of the aforementioned submatrices, the eigenvalues (λ_1, λ_2) and eigenvectors $(\boldsymbol{v}_1, \boldsymbol{v}_2)$ yield

$$q_{i,j} = \begin{bmatrix} \sigma_i^2 & \sigma_{i,j} \\ \sigma_{i,j} & \sigma_j^2 \end{bmatrix} \rightarrow \quad q_{i,j} = \sum_{k=1}^{2} \lambda_k \boldsymbol{v}_k \boldsymbol{v}_k^T. \tag{5}$$

Based on the decomposition results, the error ellipses are then formed: with λ_1, λ_2 as their semimajor and minor axes elongated in the direction specified by the corresponding eigenvectors. The inspection of the minor to major axis ratio of the ellipse indicates the condition number of estimation in respective parameter subspace, while its orientation represents the parameter correlation. Trivially, in case of extreme correlation, the two directions cannot be separately resolved. In ideal cases where the parameters are retrieved with equal precision and are statistically independent (uncorrelated), the ellipse becomes a circle. Therefore, in the following sections, the error ellipses are used as a concise visual interpretation tool for error analysis of the different geometrical scenarios.

TABLE I
INVESTIGATED GEOMETRICAL COMBINATION SCENARIOS AND THE RESULTED 3-D PERFORMANCE AT THE EQUATOR ($\sigma_{\mathrm{LOS}} = 19$ mm)

Case	Fusion Scenario	Heading ang. (at Equator)	Look ang.	3D precision [cm]
I	Cross-Heading	-12°	35°	σ_e: 2.46
	Right-looking	-168°	35°	σ_n: 60.6
	Asc. R.	-12°	25°	σ_v: 7.99
II	Cross-Heading	37°	35°	σ_e: 3.00
	Right-looking	143°	35°	σ_n: 21.0
	incl = 50°	37°	25°	σ_v: 7.99
III	Cross-Heading	-12°	35°	σ_e: 2.46
	Right-looking	-168°	35°	σ_n: 8.07
	Asc. R. $\theta_{sq} = 20°$	-12° (+36°)	35° (-6°)	σ_v: 1.42
IV	Cross-Heading	-12°	35°	σ_e: 2.46
	Right-looking	-168°	35°	σ_n: 11.5
	Asc. L.	-12	-35°	σ_v: 1.68
V	Cross-Heading	-12°	35°	σ_e: 2.43
	Right+Azimuth	-168°	35°	σ_n: 56.9
	Shifts (10 m)	-12°	25°	σ_v: 7.53
VI	Cross-Heading	-12°	35°	σ_e: 2.31
	Right+Azimuth	-168°	35°	σ_n: 29.2
	Shifts (2 m)	-12°	25°	σ_v: 4.04

III. EFFECT OF ORBIT AND ACQUISITION GEOMETRY

This section focuses on the effect of variation of geometry on the 3-D performance in a pure interferometric approach. The heading angle is measured clockwise from the local north direction to the projection of the satellite trajectory on the ground. The local north direction depends on the geodetic location of the imaged scene, while the projection of the satellite track changes with the inclination of the orbit and the satellite attitude (causing the squint angle) [13]. We fix the first variable by considering the 3-D performance at the equator, where the worst precision is expected, and analyze the effect of satellite orbit and squint angle (see [1] for a thorough study on the effect of look angle).

To keep the investigated cases comparable, a basic observation scenario comprising three acquisitions from cross-heading tracks is assumed in the entire analysis. The first two acquisitions are fixed to cross-heading tracks both acquired from right-looking, while the third is altered according to each specific case. For comparison purposes, the *nominal* all right and left and right-looking acquisition combinations are considered as well (Table I; cases I and IV, respectively). The investigated cases are summarized in Table I and are elaborated throughout this letter. Fig. 1 provides the 3-D LOS unit vectors of the different acquisitions of Table I projected to the 2-D local planes. The projection of the 2-D LOS vectors to each of the given axis of the local planes indicates their sensitivity to the corresponding motion component.

We consider an L-band SAR ($\lambda = 23.9$ cm) with an average coherence of 0.4 and $N = 10$ samples for calculation of the measurements' stochastic model and neglect the atmospheric

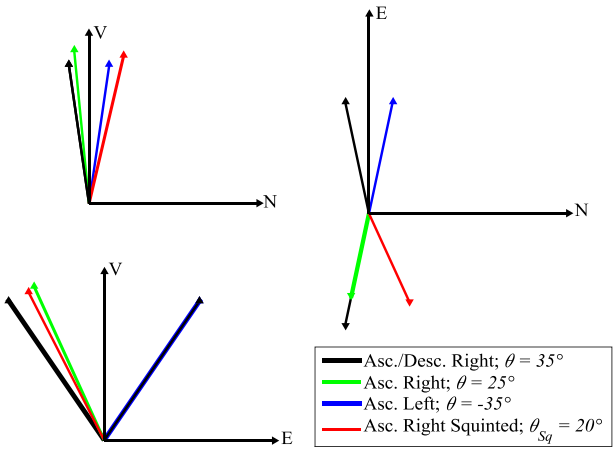

Fig. 1. Projection of the 3-D LOS of the different acquisition geometries of Table I on the 2-D local planes; the projection of each vector on the E-, N-, and V-axes indicates the sensitivity of LOS to the corresponding component. Note that the squinted acquisition improves the sensitivity to the north component.

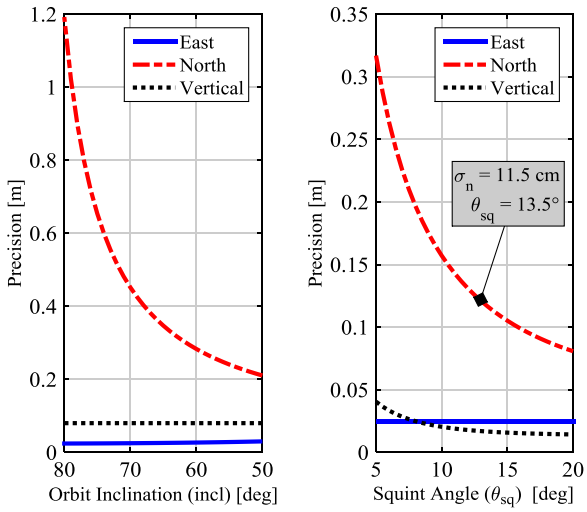

Fig. 2. Impact of changing the geometry on the achievable 3-D precision, by (left) variation of the inclination of the orbital plane and (right) variation of the squint angle; 13.5° of squint (equivalent to a yaw rotation of 24°) will yield similar performance as a left-looking configuration.

errors. This yields a ranging accuracy of 19 mm [according to (2)]. A variation of the coherence level or the number of independent samples merely has a scaling effect on the error analysis.

A. Orbit Design and Increasing the Satellite Heading Angle

The first option to improve the sensitivity to the north component is to increase the heading angle, which is in direct relation to the orbital inclination. The current SAR missions are in near-polar sun-synchronous orbits. This orbit design allows negligible variation of inclination. In order to benefit from this variation in 3-D performance, we relax the near-polar sun-synchronous orbit design and allow the variation of inclination in [50° to 80°] range for a typical low Earth orbit (LEO) of 0.001 eccentricity in 700-km altitude. The heading angle would consequently vary, leading to the gain in the sensitivity to the north direction and hence the 3-D performance. As an illustration, we consider the basic combination scenario with all right-looking acquisitions affected by an orbit of varying inclination and show the 3-D performance in Fig. 2, left. The figure indicates the performance gain in retrieving the north component when going to *mid-inclined orbit* regimes. Such orbit design, however, limits the latitudinal imaging coverage. Table I case II reports the 3-D precision for an inclination of 50°.

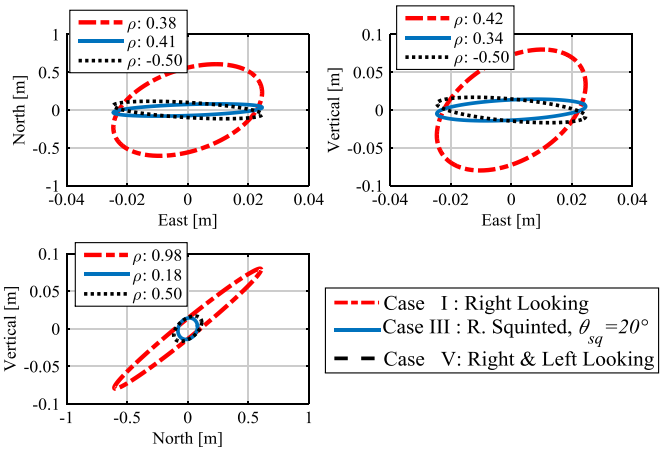

Fig. 3. Comparison of the different acquisition scenarios via the error ellipses and parameter correlations; the extreme correlation of the north–vertical plane is reduced by considering the left-looking or squinted acquisition.

B. Squinted Acquisition and Increment of the Angular Diversity

Instead of increasing the heading angle via changing the orbit design, the angular diversity of the involved acquisitions can be enhanced by steering the radar beam away from the zero-Doppler plane, leading to squinted acquisitions.

Having the nominal combination scenario (case I) and fixing to a typical orbit (eccentricity: 0.001, altitude: 700 km, inclination: 98.158°), we assess the effect of a squinted acquisition by squinting the third right-looking acquisition in the range $\theta_{sq} = [5°, 20°]$. The heading and look angles change accordingly by $\Delta\alpha$ and $\Delta\theta$, as follows:

$$\Delta\alpha \approx \operatorname{asin}\left(\sin\theta_{sq}/\sin\theta\right) \tag{6}$$

$$\Delta\theta \approx \operatorname{atan}(\tan\theta\cos\Delta\alpha) - \theta. \tag{7}$$

Fig. 2 (right) depicts the 3-D precision as a function of the squint angle, revealing the performance gain of the north component when increasing this angle.

Table I enables comparing the performance of the squinted geometry with $\theta_{sq} = 20°$ (case III) to the nominal geometric scenarios (cases I and IV) as well as the mid-inclined orbit with incl $= 50°$ (case II). As apparent, the squinted acquisition enables a performance gain beyond the limits of the other possible geometric scenarios, especially in retrieving the critical north component. For a comprehensive error analysis, the error ellipses of the mentioned cases are depicted in Fig. 3. Inspecting the error ellipses of the nominal right-looking scenario (case I) reveals a strong correlation between the north and vertical components. This leads to ambiguity in the separation of the motion components in this plane. The mentioned correlation is decreased when considering the left or squinted acquisitions, showing a better resolving performance for the latter.

Based on the comparisons, the squinted acquisition proves to outperform the possible acquisition geometries while avoiding

the challenges of the left-looking configuration or change of the orbit design. The tradeoff here is, however, at (In)SAR data processing level in the presence of high squint angle [13]. This issue is shortly addressed in the following.

IV. Squinted Acquisition, Options, and Challenges

There are two basic ways to realize a squinted geometry with a SAR: mechanical and electronic squints (or a combination of the two). In the first case, the platform undergoes a rotation about the yaw axis. Note that this option entails a variation of the Doppler centroid within the swath, which needs to be considered in processing. The Doppler centroid will be

$$f_{\mathrm{DC}} = \frac{2v}{\gamma} \sin \alpha_{\mathrm{yaw}} \sin \theta \tag{8}$$

which yields a variation between 15 and 26 kHz, from near to far range (25°–45° of incidence) for a 36° yaw rotation of an L-band system, with the LEO velocity v. Such a variation should be compared with a typical Doppler bandwidth of 1 kHz for azimuth resolutions on the order of 10 m. To minimize the Doppler variation within the swath, it is possible to introduce a pitch rotation [14], [16], but then, the heading of the LOS projection on the ground will not be constant across the swath.

This is also the case of the second option for squinting: the electronic steering. A phase ramp along the antenna will center the beam on a constant-Doppler cone (assuming the default system was totally zero steered [14], [16]), which corresponds to different headings of the LOS projection on the ground. Electronic steering requires dedicated hardware or phased arrays with adequately small element spacing to avoid the formation of strong grating lobes. The squinted geometry will pose additional requirements on timing and azimuth positioning of the sensor. A positioning error Δ_{az} will translate into a range error (thus a phase error) of $\Delta_{rg} = \Delta_{az} \sin \theta_{sq}$. In practice, only range and azimuth variations of Δ_{rg} will be relevant since a constant offset produces only a phase bias.

Concerning SAR processing, squinted acquisitions may require the introduction of special focusing strategies. The Doppler rate will vary with topography, inducing phase and defocusing effects. Both can be accommodated in a postprocessing step (see [15]). In practice, if the normal baselines are small enough, such corrections might be even unnecessary since most of the errors cancel out in the formation of interferograms, being only dependent on the geometry.

References [6] and [7] have addressed the feasibility of squinted SAR processing, through simulations and experiments with TerraSAR-X, respectively. Note that the proposed squint angle of 20° by this letter corresponds to ∼20-kHz Doppler centroid frequency for L-band, which has been proved to be feasible by experiments with TerraSAR-X [7].

A. Options of Acquiring Squinted SAR Geometries

Assuming $\Delta\theta^\circ$ diversity between the ascending acquisitions and keeping the descending passes at zero-Doppler geometry, the angular diversity can be achieved either by an extreme squinting of an ascending track by $\theta_{sq} = \Delta\theta^\circ$ every second pass or by lower squinting each ascending track once in a forward $\theta_{sq} = -\Delta\theta^\circ/2$ and once in a backward manner $\theta_{sq} = +\Delta\theta^\circ/2$. The former has the advantage of maintaining zero-Doppler geometry for every second ascending acquisition and the disadvantage of an extreme squinting at every second track. The latter has the benefit of lower squinting at each ascending pass but the drawback of slight performance loss compared to the extreme squinting scenario (Table II). However, both strategies limit the interferometric stacking possibilities of the ascending tracks to the acquisitions with similar squinting.

TABLE II
Three-Dimensional Performance of Two Different Squinting Strategies

Acquisition Scenario	Acquisition Mode	Heading ang.	Look ang.	3D precision
Extreme Squinting $\theta_{sq} = 20°$	Asc. R.	-12°	35°	σ_e: 2.46
	Desc. R.	-168°	35°	σ_n: 8.07
	Asc. R. Squinted	-12° (+36°)	35° (-6°)	σ_v: 1.42
Forward-Backward Squinting $\theta_{sq} = \pm 10°$	Asc. R. Squinted	-12° (+17°)	35°(-2°)	σ_e: 2.22
	Desc. R.	-168°	35°	σ_n: 8.41
	Asc. R. Squinted	-12° (-17°)	35°(-2°)	σ_v: 1.85
Forward-Backward Squinting $\theta_{sq} = \pm 20°$	Asc. R. Squinted	-12° (+36°)	35° (-6°)	σ_e: 2.57
	Desc. R.	-168°	35	σ_n: 4.90
	Asc. R. Squinted	-12° (-36°)	35° (-6°)	σ_v: 1.46

Considering the constellation of two satellites, e.g., TerraSAR-X/TanDEM-X or the proposed TanDEM-L mission [8], the aforementioned acquisition strategies may be extended. For instance, one satellite may only be fixed to forward squinting and the other to backward at all ascending tracks. This option enables the instantaneous 3-D retrieval at each revisit: with the drawback of noncoherent acquisitions between the two satellites and the advantage of full stacking capability at all ascending tracks. The alternative for keeping the acquisitions coherent between the two satellites would be to apply the aforementioned fore- and backward squinting plan to each. Table II summarizes the 3-D performance of different acquisition plans. The further improvement of 3-D performance by considering the fore- and backward squints of $\pm 20^\circ$ is evident.

V. Effect of Measurement Fusion

Being projected to the ATD, the azimuth shifts are geometrically complementary to the interferometric measurements. The quality of the azimuth shifts, however, is limited by SAR azimuth resolution, and the relative contribution of the shifts compared to the interferometric measurements is merely governed by the ratio of the azimuth resolution to half of the wavelength [12]. Therefore, the fusion of azimuth shifts is only advantageous in cases of long-wavelength SAR with high azimuth resolution.

To show the 3-D performance, integration of azimuth shifts to the nominal right-looking combination scenario of case I is considered. We compare two extreme cases, with azimuth resolutions (ρ_{az}) of 10 and 2 m (Table I, cases V and VI, respectively). An L-band SAR with a coherence of 0.4 and ten independent samples are assumed in the estimation of the quality of measurements [according to (2) and (3)]. Comparison of the results (Table I) indicates that the integration of azimuth shifts can enhance the 3-D performance. As expected, the extent of this improvement is governed by the azimuth resolution.

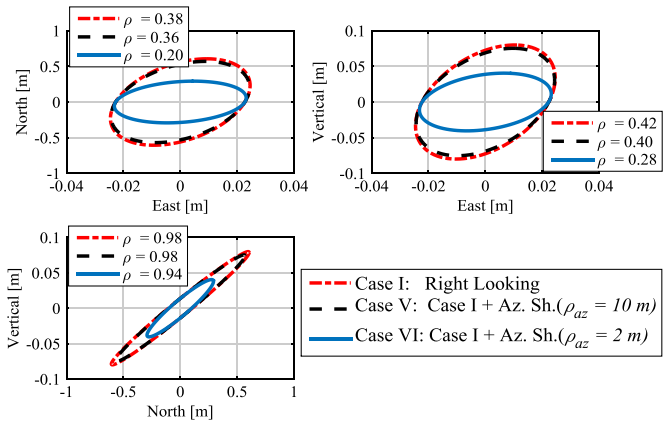

Fig. 4. Comparison of performance in integration of the InSAR and azimuth shifts, considering two cases with azimuth resolutions of 10 and 2 m.

Fig. 4 depicts the corresponding error ellipses, indicating that, even in case of high azimuth resolution, the extreme north–vertical correlation may not be resolved.

VI. Discussion and Conclusion

Assessing the different geometric possibilities in this letter, the squinted acquisition was shown to be an optimum choice for improving the precision of 3-D motion retrieval. This geometry was proved to outperform the left-looking configuration as well as the mid-inclined orbit geometry, not only in improving the precision of retrieving the critical north component but also in resolving the high correlation (ambiguity) between the north and vertical motion components. The 3-D performance with squinted configuration will be further improved by integrating the ATD measurements via exploiting the widely separated Doppler spectra as suggested by [7] and exploited in [6].

As a follow-up study, the effect of the improved 3-D retrieval on the performance of InSAR-based hazard monitoring in case of volcanic and seismic deformations is shortly addressed in [4], and it will be further investigated in future work.

References

[1] F. Rocca, "3D motion recovery with multi-angle and/or left right interferometry," in *Proc. 3rd Int. Workshop ERS SAR*, 2003, pp. 1–5.

[2] T. J. Wright, B. E. Parsons, and Z. Lu, "Toward mapping surface deformation in three dimensions using InSAR," *Geophys. Res. Lett.*, vol. 31, no. 1, Jan. 2004, Art. ID L01607.

[3] E. Erten, A. Reigber, and O. Hellwich, "Generation of three-dimensional deformation maps from InSAR data using spectral diversity techniques," *ISPRS J. Photogramm. Remote Sens.*, vol. 65, no. 4, pp. 388–394, Jul. 2010.

[4] H. Ansari *et al.*, "InSAR sensitivity analysis of TanDEM-L mission for modeling volcanic and seismic deformation sources," in *Proc. FRINGE Workshop*, Frascati, Italy, Mar. 23–27, 2015, pp. 1–8.

[5] J. Hu *et al.*, "Resolving three-dimensional surface displacements from InSAR measurements: A review," *Earth-Sci. Rev.*, vol. 133, pp 1–17, Jun. 2014.

[6] H. Jung, Z. Lu, A. Shepherd, and T. Wright, "Simulation of the SuperSAR multi-azimuth synthetic aperture radar imaging system for precise measurement of three-dimensional Earth surface displacement," *IEEE Trans. Geosci. Remote Sens.*, vol. 53, no. 11, pp. 6196–6206, Nov. 2015.

[7] J. Mittermayer *et al.*, "Bidirectional SAR imaging mode," *IEEE Trans. Geosci. Remote Sens.*, vol. 51, no. 1, pp. 601–614, Jan. 2013.

[8] A. Moreira *et al.*, "TanDEM-L: A mission proposal for monitoring dynamic Earth processes," in *Proc. IEEE IGARSS*, Jul. 24–29, 2011, pp. 1385–1388.

[9] R. Scheiber and A. Moreira, "Coregistration of interferometric SAR images using spectral diversity," *IEEE Trans. Geosci. Remote Sens.*, vol. 38, no. 5, pp. 2179–2191, Sep. 2000.

[10] N. B. D. Bechor and H. A. Zebker, "Measuring two-dimensional movements using a single InSAR pair," *Geophys. Res. Lett.*, vol. 33, no. 16, 2006, Art. ID L16311.

[11] R. Bamler and P. Hartl, "Synthetic aperture radar interferometry," *Inv. Prob.*, vol. 14, no. 4, pp. R1–R54, 1998.

[12] R. Bamler and M. Eineder, "Accuracy of differential shift estimation by correlation and split-bandwidth interferometry for wideband and delta-k SAR systems," *IEEE Geosci. Remote Sens. Lett.*, vol. 2, no. 2, pp. 151–155, Apr. 2005.

[13] I. G. Cumming and F. H. Wong, *Digital Processing of Synthetic Aperture Radar Data: Algorithms and Implementation*. Norwood, MA, USA: Artech House, 2005.

[14] H. Fiedler, E. Boerner, J. Mittermayer, and G. Krieger, "Total zero Doppler steering—A new method for minimizing the Doppler centroid," *IEEE Geosci. Remote Sens. Lett.*, vol. 2, no. 2, pp. 141–145, Apr. 2005.

[15] M. Rodriguez-Cassola *et al.*, "Doppler-related distortions in TOPS SAR images," *IEEE Trans. Geosci. Remote Sens.*, vol. 53, no. 1, pp. 25–35, Jan. 2015.

[16] D. P. Scharf, "Analytic yaw-pitch steering for side-looking SAR with numerical roll algorithm for incidence angle," *IEEE Trans. Geosci. Remote Sens.*, vol. 50, no. 9, pp. 3587–3594, Sep. 2012.